

Single-Crystal Elasticity of MgSiO₃ Bridgmanite to Mid-Lower Mantle Pressure

**Key Points:**

- We measured both compressional and shear wave velocities of MgSiO₃ bridgmanite up to mid-lower mantle pressure for the first time
- The effect of chemistry on the elastic moduli and elastic anisotropy of bridgmanite at lower mantle pressures is discussed
- We compare the seismic velocities for a simplified primitive upper mantle composition with 1D seismic models of Earth's lower mantle

Supporting Information:

Supporting Information may be found in the online version of this article.

Correspondence to:

G. Criniti,
giacomo.criniti@uni-bayreuth.de

Citation:

Criniti, G., Kurnosov, A., Ballaran, T. B., & Frost, D. J. (2021). Single-crystal elasticity of MgSiO₃ bridgmanite to mid-lower mantle pressure. *Journal of Geophysical Research: Solid Earth*, 126, e2020JB020967. <https://doi.org/10.1029/2020JB020967>

Received 10 SEP 2020

Accepted 11 APR 2021

Giacomo Criniti¹ , Alexander Kurnosov¹ , Tiziana Boffa Ballaran¹ , and Daniel J. Frost¹ 

¹Bayerisches Geoinstitut, University of Bayreuth, Bayreuth, Germany

Abstract The combination of seismic observations and mineral physics data represents a unique tool to understand the structure and evolution of the deep Earth's interior. However, to date, elasticity data on both compressional (v_p) and shear (v_s) wave velocities of MgSiO₃ bridgmanite are limited to shallow mantle conditions, hampering the resolution of mineral physics models. Here, we report the first single-crystal measurements of v_p and v_s of MgSiO₃ bridgmanite up to ~79 GPa using high-pressure Brillouin scattering and single-crystal X-ray diffraction in a diamond anvil cell. At shallow lower mantle pressures, the elastic anisotropy of MgSiO₃ bridgmanite was found to be similar, albeit smaller than that of Fe,Al-bearing bridgmanite of Kurnosov et al. (2017) but differed significantly from that proposed in the recent study of Fu et al. (2019). Using the elastic stiffness coefficients of bridgmanite obtained in this study at different pressures, we calculate the pressure dependence of the adiabatic bulk modulus, $K_{S0} = 257.1(6)$ GPa, $K'_{S0} = 3.71(4)$, and of the shear modulus, $G_0 = 175.6(2)$ GPa, $G'_0 = 1.86(1)$. These elastic parameters are included in a self-consistent thermodynamic model to calculate seismic wave velocities along a lower mantle adiabat for a primitive upper mantle bulk composition in the FeO-CaO-MgO-SiO₂ system, which is currently the most complex system for which sufficient data exist. This preliminary model provides a good match to the v_s and v_p of 1D seismic models, implying that the composition of the lower mantle may be closer to pyrolite, rather than being more bridgmanite rich.

1. Introduction

While it is accepted that the lower mantle phase assemblage is comprised primarily of Al- and Fe-bearing MgSiO₃ bridgmanite, the exact proportion and the bulk composition of the lower mantle as a whole remain uncertain. The abundance of bridgmanite relative to ferropericlase will be controlled by the bulk Mg/Si ratio. In a pyrolite composition, which is believed to represent the average composition of the upper mantle (Ringwood, 1962), this ratio is ~1.3 and a pyrolytic lower mantle assemblage would be comprised of ~78% bridgmanite, 15% ferropericlase, and 7% calcium perovskite by volume (e.g., Irifune, 1994; Irifune et al., 2010; Ishii et al., 2011). The Earth is frequently proposed to have formed from carbonaceous chondrites, however, which have a Mg/Si ratio much closer to 1.0 (Palme & O'Neill, 2004). Aside from Si potentially entering the Earth's core (e.g., Poirier, 1994; Wänke, 1981), one way to explain the Mg/Si ratio of the upper mantle is if the lower mantle is richer in bridgmanite as a result of fractional crystallization during the magma ocean stage of Earth's history (e.g., Ballmer et al., 2017; Elkins-Tanton, 2012; Tonks & Melosh, 1993). This scenario is supported by shear wave velocity measurements of MgSiO₃ and Al-bearing bridgmanite at pressures over 1 Mbar (Murakami et al., 2012), for which comparison with the PREM seismic velocity model indicates a lower mantle containing at least 93 vol% of bridgmanite.

In the previous studies of Murakami et al. (2007, 2012), performed in the DAC using Brillouin scattering measurements, it was not possible to directly measure values of v_p , which were instead estimated using bulk modulus determinations from previous static compression measurements (Fiquet et al., 2000). This potential cause of uncertainty arises in high pressure Brillouin scattering measurements because the v_p signal overlaps with the much more intense v_s signal of the diamond anvils. This effect is particularly pronounced for polycrystalline samples (Murakami et al., 2007, 2012), where the sample peaks are broad and tend to overlap with diamond even at ambient pressure. To overcome this problem, Fu et al. (2019) combined Brillouin scattering measurements of v_s with impulsive stimulated light scattering (ISLS) measurements for v_p to examine bridgmanite single crystals at 25 and 35 GPa, because ISLS has the advantage that the signal originating from the sample does not overlap with that of the diamond anvils. Fu et al. (2019) studied two bridgmanite samples with different Fe and Al contents. The determined bridgmanite elastic anisotropy

© 2021. The Authors.

This is an open access article under the terms of the [Creative Commons Attribution License](https://creativecommons.org/licenses/by/4.0/), which permits use, distribution and reproduction in any medium, provided the original work is properly cited.

is different, however, from that measured by Kurnosov et al. (2017), who performed simultaneous Brillouin scattering and single crystal X-ray diffraction measurements on Fe- and Al-bearing bridgmanite up to ~40 GPa. To date, no direct experimental constraints exist on v_p of bridgmanite at pressures of the mid lower mantle and although a number of computational studies have been performed, they partially disagree with one another due to different choices in the potentials and approximations used (Oganov et al., 2001; Wentzcovitch et al., 1998, 2004; Zhang et al., 2013). For instance, both compressional and shear wave velocities calculated at high pressure and room temperature by Oganov et al. (2001) are 2%–3% faster than those reported by Wentzcovitch et al., (2004). Results from ultrasonic measurements by Chantel et al. (2012) at low pressure seem to agree with the v_p of Wentzcovitch et al. (2004) and the v_s of Oganov et al. (2001), while the v_s of Murakami et al. (2007) are in good agreement with those of Wentzcovitch et al. (2004).

In this study, we show that single-crystal DAC elasticity measurements can provide some constraints on the v_p of MgSiO_3 bridgmanite even at shallow lower mantle pressures, if the in-plane orientation of the crystal is correctly chosen. Because both the diamond anvils and the sample are single crystals, their sound wave velocities depend on the wave propagation direction. If the minimum of the v_p of the sample matches the maximum of the v_s of the diamond, it is possible to observe a portion of the dispersion curve of bridgmanite even at shallow lower mantle pressure (~30 GPa). At higher pressure, the v_p overlaps completely with the diamond v_s , as the sample has higher pressure derivatives of the elastic moduli than diamond. At deep lower mantle pressures, however, a crossover occurs, and the v_p of bridgmanite appears at higher frequency (i.e., velocity) than the v_s of the diamond in the Brillouin spectrum and, therefore, can be observed again. In this study, we have conducted single-crystal X-ray diffraction and Brillouin scattering measurements on four crystals of MgSiO_3 bridgmanite in the DAC up to pressures of the middle lower mantle. Combining all elasticity and density measurements in a global fit (Buchen, 2018), we self-consistently determine, for the first time, the full elastic tensor of MgSiO_3 bridgmanite at mid lower mantle pressures. The newly determined values of the elastic moduli and their pressure derivatives are used to update existing mineral physics models and estimate seismic velocities for a lower mantle with a pyrolite bulk composition.

2. Materials and Methods

Single crystals of MgSiO_3 bridgmanite were synthesized at 25 GPa and 1573 K (Boffa Ballaran et al., 2012) in a multianvil large volume press (LVP). Inclusion free bridgmanite crystals were selected for which sharp X-ray diffraction peak profiles (full width half maxima < 0.12°) were obtained in omega-scan rotations. Suitable crystals were then oriented and polished on both sides to platelets with a thickness of 8–10 μm . High-pressure single-crystal X-ray diffraction and Brillouin spectroscopy measurements were performed in a BX90 piston-cylinder-type DAC (Kantor et al., 2012). (100)-oriented Boehler-Almax type Ia diamond anvils were combined with Boehler-Almax seats to achieve opening angles larger than 80° (Boehler & De Hantsetters, 2004). The diameter of the diamond culets was 400 or 350 μm for measurements up to ~35 GPa, and 250 μm for measurements at higher pressure. Before gluing the diamond anvils, Brillouin scattering measurements were performed on the two diamonds to identify the v_s dispersion curves relative to the orientation of each diamond. By rotating one of the two diamonds with respect to the other, it was possible to align their dispersion curves and, therefore, minimize the effective width of the diamond v_s peak in the Brillouin spectra. Re gaskets were indented to a thickness of ~60 and ~35 μm for target pressures of 35 and 80 GPa, respectively. Ne or He were loaded as quasi-hydrostatic pressure transmitting media using a gas loading apparatus (Kurnosov et al., 2008).

High-pressure Brillouin scattering experiments conducted in platelet geometry (Speziale et al., 2014; Whitfield et al., 1976) require at least two different platelet orientations to solve for the nine independent elastic stiffness components, c_{ij} , of an orthorhombic crystal such as bridgmanite. This is achieved by combining experimentally measured density and sound wave velocities to fit the Christoffel's equation (e.g., Every, 1980):

$$\left| c_{ijkl}q_jq_l - \rho v_i^2 \delta_{ik} \right| = 0 \quad (1)$$

where c_{ijkl} are the elastic stiffness components (tensorial notation, see supporting information S1), q_j and q_l are direction vectors, ρ is density, v_i are the sound wave velocities and δ_{ik} is the Kronecker delta. Three

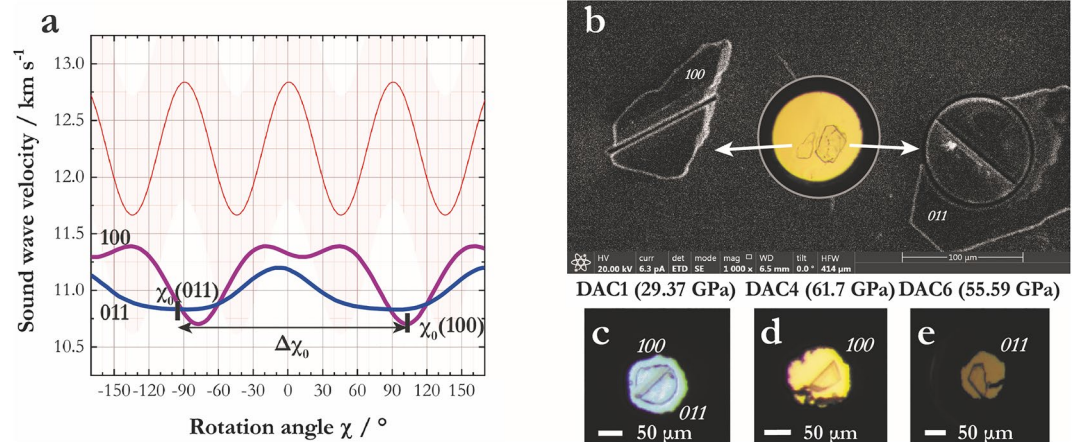


Figure 1. (a) Schematic representation of the ideal orientation of the v_p of platelets (100) (purple) and (011) (blue) relative to each other and to the diamond v_s (red) at room pressure. The shaded pink area represents the predicted full width of the diamond peak at high pressure (see supporting information S1), where the v_p of the samples cannot be resolved. Note that the diamonds have been aligned in such a way to produce only one v_s signal at each orientation. The difference in rotation angle ($\Delta\chi_0$) between the g_0 vectors of the two crystal platelets was used together with the UB matrix of the crystals to calculate the desired FIB cutting pattern. (b) Photograph of the two platelets 100 and 011 before FIB cutting in a test DAC (middle circular inset) and secondary electron image of the same platelets after FIB cutting. (c–e) Photographs of platelets 100 and 011 inside the relevant sample chambers at high pressure, loaded with Ne (c) or He (d and e) gas.

sets of high-pressure experiments (runs) were performed employing two different sets of bridgmanite single-crystal platelets with different orientations. In the first run, crystals with Cartesian indices (0.81, 0.49, 0.31) and (0.35, 0.16, 0.92), were selected based on the low extent of c_{ij} correlation at ambient conditions (for a more detailed description, see supporting information S1). These crystals were loaded into two separate DACs and Brillouin scattering and X-ray diffraction measurements were performed up to ~ 35 GPa. At this pressure, even the slowest bridgmanite v_p values overlapped with the v_s of the diamond anvils, leaving many c_{ij} values unconstrained. To overcome this limitation two further runs were performed using a second set of single crystal platelets with orientations chosen to maximize the appearance of the v_p signals on either side of the diamond v_s peak. The platelet orientations were first selected by simulating the velocities for different crystal planes using published c_{ij} values (Sinogeikin et al., 2004). To simulate realistic datasets, synthetic velocities were scattered by randomly adding up to ± 40 m/s to v_s and 70 m/s to v_p , which are values comparable to our estimated experimental uncertainties. Platelets with Cartesian indices (0.00, 0.80, 0.55) and (1.00, 0.00, 0.00), which correspond to the (011) and (100) crystallographic planes, were found to be optimal based on the low correlation between the c_{ij} s (supporting information S1). These orientations also have relatively slow and fast v_p respectively, such that the direction of the v_p maximum in the (100) plane could be aligned with the diamond v_s minimum, while the v_p minimum in the (011) plane could be aligned with the diamond v_s maximum, to maximize the pressure interval over which these signals could be visible (Figure 1a). To load two crystals into the same DAC, while also maximizing their dimensions with respect to the gasket hole dimension, it was necessary to cut them into semicircular-shaped platelets, which meant that both crystals had to be correctly aligned relative to the diamonds and to each other before cutting. Two double-sided-polished but unshaped platelets in the selected planes were, therefore, first placed on a diamond anvil (Figure 1b) and the desired orientations relative to the diamonds were then determined for each crystal using single-crystal X-ray diffraction. The two single-crystal platelets were then cut into semi-circles for loading into the DAC (Figure 1b) using a FEI Scios focused ion beam (Schulze et al., 2017), while maintaining the required orientations relative to the straight edges. Ion beam cutting was performed using a beam current of 3 nA at an acceleration voltage of 30 kV. According to the target pressure, one or two platelets were loaded into the DAC sample chamber together with a ruby chip for preliminary pressure determination (Figures 1c–1e). Before gas loading, the bridgmanite crystals were rotated on the diamond culet using a needle, until the desired orientations (determined by means of XRD) relative to the diamond

anvils were achieved. The two crystals were loaded together in the same DAC for measurements up to ~30 GPa (second run), and in two separate DACs for measurements above 50 GPa (third run).

Brillouin scattering measurements were performed using the system installed at the BGI (Trots et al., 2013). The system employs a Coherent Verdi V2 solid-state Nd:YVO₄ laser with a 532 nm single wavelength output and a six-pass Sandercock-type piezoelectrically driven scanning tandem Fabry-Pérot interferometer (Sandercock, 1982) equipped with a single pixel photon counter detector (Hamamatsu C11202-50). A laser power of 100–200 mW was used, which corresponds to 40–80 mW before entering the DAC. The scattering angle between the incident and the analyzed laser beam, equal to 80°, was calibrated using a fused silica glass standard. Further details concerning the system alignment and calibration, as well as a discussion of potential errors related to misalignment, are discussed in supporting information S1. Simultaneous density measurements were performed on a Huber Eulerian single-crystal diffractometer coupled with an ultra-high intensity rotating anode X-ray source FR-E + SuperBright from Rigaku equipped with multi-layer VaryMax™ focusing optics (MoK α radiation) (Trots et al., 2011). The rotating anode was operated at 45 kV and 55 mA, and the diffractometer was driven by the SINGLE software (Angel & Finger, 2011). Cell parameters were determined and refined with the vector least-squares method (Ralph & Finger, 1982), using up to 15 unique reflections centered in eight positions (King & Finger, 1979) to eliminate the effect of crystal offsets and diffractometer aberrations. To reduce the very long counting times required when using a point detector on small crystals at very high pressures, density measurements above 50 GPa were conducted on a Kappa-geometry Oxford Diffraction single-crystal X-ray diffractometer (Xcalibur2) equipped with a Sapphire 2 CCD area detector. The diffractometer uses graphite-monochromatized MoK α radiation ($\lambda = 0.70937 \text{ \AA}$) and was operated at 50 kV and 40 mA. At each pressure point, intensity data collections of ~24 h with 60 s of exposure time were performed, and lattice parameters were determined from at least 100 reflections.

3. Results

3.1. Sound Wave Velocities of MgSiO₃ Bridgmanite at High Pressure

Sound wave velocities of MgSiO₃ bridgmanite were measured at 14 pressure points, ranging from ambient pressure to 78.8(5) GPa (Table 1) over the three different sets of runs. Typical Brillouin spectra in the low- and high-pressure range (Figure 2a) show the progressive overlap between the v_p of bridgmanite and v_s of diamond, with a crossover taking place at pressures above 50 GPa. To our knowledge, these are the first direct measurements of P-wave velocities of MgSiO₃ bridgmanite at deep lower mantle pressures, albeit that the v_p of bridgmanite could be observed only in certain ranges of rotation angle (χ) at such high pressures. Usually Equation 1 is solved using the appropriate number of acoustic velocities collected at each individual pressure point, which in the case of an orthorhombic crystal, such as bridgmanite, requires the measurement at the same conditions of at least two differently oriented crystals. This procedure is hereinafter referred to as an individual fit.

Individual fits of the measured sound velocity data from the first run do not converge at pressures higher than 15 GPa because of the limited number of directions where v_p was observed. In the second run, both minima and maxima of the v_p of the two platelets were visible up to 19.40(3) GPa, whereas at higher pressure the maximum of the v_p of both platelets completely overlapped with the diamond peak. It was still possible to obtain an individual fit at a pressure of ~30.3 GPa by combining sound velocities collected on 4 different platelets from the first and second run in a small pressure range between 29.37(5) and 31.20(6) GPa (Table 1).

It is evident that this approach cannot be applied at very high pressure, where some of the c_{ij} s are poorly constrained due to the lack of observations (supporting information S1). For this reason, we have used the same approach proposed by Kurnosov et al. (2017) and described in detail in Buchen (2018), which consists of fitting all sound velocity and density data with finite strain equations of state (EOS) describing the evolution with pressure of each c_{ij} , using the formalism of Stixrude & Lithgow-Bertelloni (2005):

Table 1
Elastic Stiffness Coefficients (c_{ij}) and Elastic Moduli From Individual Fits and Global Fit, Reported in GPa

P (GPa)	ρ (g cm ⁻³)	c_{11}	c_{22}	c_{33}	c_{44}	c_{55}	c_{66}	c_{12}	c_{13}	c_{23}	K_V	G_V	K_R	G_R	K_{VRH}	G_{VRH}
Individual fits																
0.00010(1)	4.1045(10)	482(3)	523(4)	468(3)	202.3(3)	182.8(10)	148.6(14)	122(3)	146(2)	154.3(14)	257.4(13)	176.8(5)	257.0(13)	174.4(5)	257.2(13)	175.6(5)
4.99(1)	4.183(4)	487(9)	580(6)	493(4)	213.3(8)	193.1(17)	160.4(11)	139(4)	149(4)	168(3)	276(2)	187.7(7)	274(2)	185.4(7)	275(2)	186.5(7)
9.32(2)	4.248(4)	535(3)	587(7)	522.5(19)	220.7(3)	198.1(7)	168.8(10)	153(4)	164(2)	170(3)	290.8(15)	194.7(5)	290.2(15)	192.9(5)	290.5(15)	193.8(5)
19.40(3)	4.390(6)	580.0(15)	643.8(8)	597.1(19)	237.1(3)	205.5(4)	189.6(8)	185.0(4)	184.2(17)	196.7(4)	328.1(16)	210.1(5)	327.3(16)	208.8(5)	327.7(16)	209.5(5)
30.3 ^a	-	622(3)	697(30)	649(6)	251.7(8)	216.3(5)	208.0(5)	211(13)	199(4)	216(14)	358(5)	224.7(15)	356(6)	223.6(15)	357(5)	224.2(15)
Global fit																
0.00010(1)	4.1045(10)	486.8(20)	524.3(26)	467.7(16)	202.3(2)	180.2(4)	141.9(5)	124.3(18)	140.9(13)	152.6(10)	257.1(8)	175.6(2)	256.7(8)	172.9(2)	256.9(8)	174.2(2)
Set 1																
4.99(1)	4.183(4)	512.7(16)	556(2)	500.3(14)	212.0(2)	187.8(4)	153.4(5)	140.9(16)	151.7(11)	163.4(9)	275.7(7)	184.9(2)	275.2(7)	182.6(2)	275.5(7)	183.7(2)
15.40(3)	4.335(4)	564.0(12)	620(2)	566.5(12)	231.1(2)	202.6(3)	176.9(4)	175.5(13)	173.8(10)	185.3(9)	313.3(5)	203.2(2)	312.6(5)	201.5(2)	313.0(5)	202.4(2)
21.63(4)	4.420(5)	593.4(13)	657(2)	605.1(13)	241.9(2)	210.9(3)	190.8(3)	196.4(13)	186.8(11)	198.2(9)	335.3(5)	213.6(2)	334.5(5)	212.3(2)	334.9(5)	213.0(2)
26.77(5)	4.487(5)	616.8(16)	687(2)	636.4(15)	250.5(2)	217.3(2)	202.0(3)	213.6(14)	197.3(13)	208.6(9)	353.2(6)	222.0(2)	352.3(6)	220.7(2)	352.7(6)	221.4(2)
31.20(6)	4.543(6)	636.5(19)	712(2)	663.1(18)	257.7(2)	222.7(2)	211.7(3)	228.5(16)	206.3(15)	217.4(10)	368.4(7)	229.0(2)	367.4(7)	227.8(2)	367.9(7)	228.4(2)
35.61(7)	4.597(6)	656(2)	737(2)	689(2)	264.8(3)	227.9(2)	221.2(3)	243.3(19)	215.2(18)	226.1(10)	383.4(8)	235.9(2)	382.3(8)	234.7(2)	382.9(8)	235.3(2)
Set 2																
9.32(2)	4.248(4)	533.5(14)	581.8(23)	526.9(13)	219.7(2)	193.9(3)	162.8(4)	154.6(14)	160.6(10)	172.2(9)	290.8(6)	192.3(2)	290.2(6)	190.3(2)	290.5(6)	191.3(2)
19.40(3)	4.390(6)	584.0(12)	645.0(21)	592.7(13)	238.4(2)	208.2(3)	186.3(3)	189.6(13)	182.6(10)	194.0(9)	328.3(5)	210.3(2)	327.5(5)	208.8(2)	327.9(5)	209.6(2)
29.37(5)	4.520(6)	627.3(17)	700.1(22)	650.7(17)	254.4(2)	220.2(2)	207.2(3)	221.5(15)	202.1(14)	213.3(9)	361.3(6)	225.8(2)	360.3(6)	224.5(2)	360.8(6)	225.1(2)
55.59(13)	4.825(6)	738(5)	845(4)	805(4)	294.7(5)	249.3(4)	263.6(5)	311(3)	254(3)	264.7(15)	449.8(13)	265.4(4)	448.1(13)	263.5(4)	449.0(13)	264.4(4)
61.7(2)	4.89(1)	761(5)	876(4)	839(4)	303.1(6)	255.2(4)	276.1(5)	331(4)	266(4)	275.9(17)	469.1(15)	273.7(4)	467.2(15)	271.4(4)	468.2(15)	272.5(4)
71.5(2)	4.99(1)	800(7)	928(5)	896(5)	317.0(7)	264.7(5)	297.3(7)	367(5)	286(5)	295(2)	502.1(18)	287.6(5)	499.8(18)	284.4(5)	501.0(18)	286.0(5)
78.8(5)	5.06(1)	825(8)	962(5)	933(6)	325.8(8)	270.6(6)	311.1(8)	390(6)	298(5)	307(2)	523(2)	296.5(5)	521(2)	292.5(5)	522(2)	294.5(5)

The numbers between brackets represent one standard deviation.

^aCombined velocities from pressure points at 29.37 GPa (set 2) and 31.20 GPa (set 1).

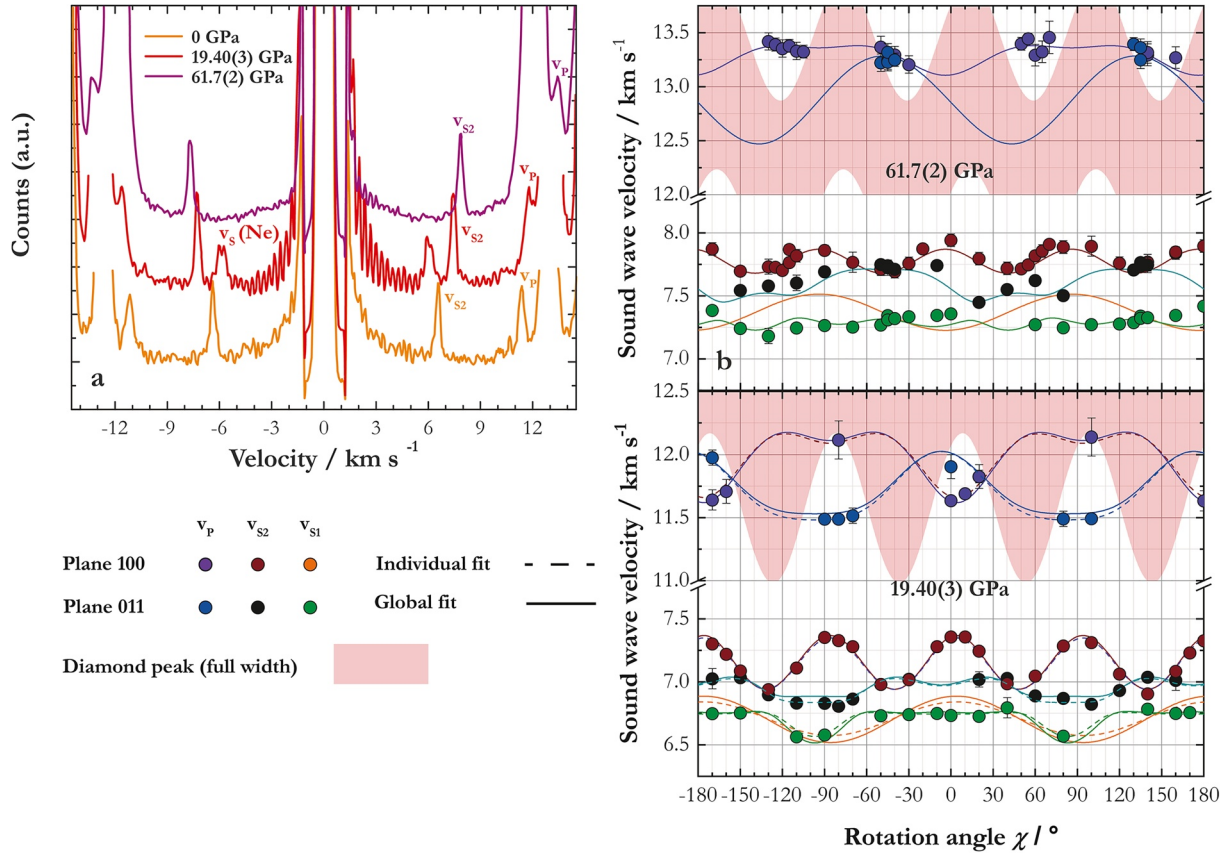


Figure 2. (a) Selected Brillouin spectra of crystal 100 at different pressures show the progressive overlap of the sample v_p with the v_s of diamond (orange and red lines), with the crossover between the two peaks taking place at pressures above ~ 50 GPa (purple line). (b) Data points and dispersion curves (solid lines) obtained from the global fit at low (top) and high (bottom) pressures. The pink shaded area represents the full width of the diamond peak, where the v_p of the sample cannot be measured. At 19.40(3) GPa, the dispersion curves from the individual fit are also plotted (dashed lines), showing excellent agreement between the two fitting procedures.

$$c_{ijkl} = (1 + 2f)^{\frac{5}{2}} \left\{ c_{ijkl,0} + (3K_0 c'_{ijkl,0} - 5c_{ijkl,0})f + \left(6K_0 c'_{ijkl,0} - 14c_{ijkl,0} - \frac{3}{2} K_0 \delta_{kl}^{ij} (3K'_0 - 16) \right) f^2 \right\} \quad (2)$$

where c_{ijkl} is the elastic stiffness component (tensorial notation, see supporting information S1) at a certain

volume, $f = \frac{1}{2} \left[\left(\frac{V_0}{V} \right)^{\frac{2}{3}} - 1 \right]$ is the finite Eulerian strain, $c_{ijkl,0}$ is the elastic stiffness component at ambient

conditions and $c'_{ijkl,0}$ its pressure derivative, K_0 is the bulk modulus and K'_0 its pressure derivative, and δ_{kl}^{ij} is -3 for c_{1111} , c_{2222} , and c_{3333} and -1 for the other six independent components of the tensor. The coefficients were fitted to the complete velocity dataset using a script implemented in the software package Origin 2019 (OriginLab corporation, Northampton, MA, USA) and described more in detail in Buchen (2018). In our fitting procedure, $c_{ij,0}$ were initially fixed to the values determined independently at ambient conditions, while $c'_{ij,0}$ were refined. Only in the last cycle, the $c_{ij,0}$ were allowed to vary and were therefore refined together with the $c'_{ij,0}$. Further details are provided in the supplementary information (supporting information S1). This approach (hereinafter referred to as a global fit) has the advantage that all velocity data from all pressure points can be used to constrain the c_{ij} , also at those pressures where data are scarce due to the challenging conditions. For instance, c_{22} is not well constrained at 30 GPa, due to the overlap of the v_p of bridgmanite with the v_s of the diamond. However, its pressure evolution is well constrained by the measurements conducted above 50 GPa, i.e., at pressures where v_p can be observed again, at least in some orientations

Table 2
EOS Parameters for K and G in the Voigt and Reuss Bound

	K_{SV}	G_V	K_{SR}	G_R	G_R	G_R	G_R
Order	3	3	3	3	3	3	4
M_0 (GPa)	257.1(6)	175.6(2)	256.7(4)	174.0(6)	173.0(3)	177.2(12)	172.8(4)
M_0'	3.71(4)	1.86(1)	3.70(3)	1.86(4)	1.92(2)	1.81(2)	1.96(2)
M_0'' (GPa ⁻¹)	<i>-0.014</i>	<i>-0.0174</i>	<i>-0.014</i>	<i>-0.0173</i>	<i>-0.0168</i>	<i>-0.0179</i>	<i>-0.0162(8)</i>
P range (GPa)	0–78.8	0–78.8	0–78.8	0–78.8	0–27.0	55.9–78.8	0–78.8

Values of M''_0 in italics are implied from third-order truncations.

on the other side of the diamond v_S . On the other hand, c_{11} is poorly constrained above 50 GPa, but its high-pressure evolution is very well constrained by measurements on 4 different platelets up to 35 GPa. This approach reduces the number of independent variables from 117 ($9 c_{ij} \times 13$ pressure points) down to 18 ($9 c_{ij,0} + 9$ pressure derivatives) while having the same number of observables. In this way, it was possible to obtain the elastic tensor of bridgmanite, within reasonable uncertainties, at all pressure points. Measured velocities in the low-pressure range (i.e., less than 30 GPa) constrain well the zero-pressure values of the c_{ij} (i.e., $c_{ijkl,0}$). If we considered only velocities measured in the low-pressure range, data scattering could still bias the third-order fit of the c_{ij} , even when a global fit is employed. This happens because the higher the pressure at which wave velocities are measured, the larger is the constraint they provide on the pressure derivative of the c_{ij} (i.e., $c'_{ij,0}$). Therefore, despite being unable to perform individual fits at pressure points higher than 30 GPa, the measured velocities at mid-lower mantle conditions are of extreme importance in the global fit procedure. Furthermore, we stress that virtually no discrepancies between the c_{ij} calculated from the finite strain EOS and the values determined using the individual fits can be observed, with values typically identical within two standard deviations (Table 1, Figure S1).

A potential downside of the global fit procedure is that we are of course assuming that the c_{ij} s follow a third-order finite strain equation, but this should be a safe assumption given the known high-pressure behavior of MgSiO₃ bridgmanite (Boffa Ballaran et al., 2012) where no phase transitions either structural or electronic occur in the pressure range investigated. Although at the highest pressure some c_{ij} s are not as well constrained (e.g., c_{11}) as others in the global fit, the constraints provided by the lower pressure data leave very little room for uncertainty, unless significant anomalous compression behavior occurs. As described in supporting information S1, we also tested global fitting using fourth-order EOSs. Although convergence in the refinement was not possible for all c_{ij} s, this led to a slightly poorer agreement with the high-pressure shear velocity data, as shown in Figure S10 and a third-order fit was, therefore, retained for all c_{ij} s. A detailed assessment of possible errors arising from the deviation of the c_{ij} of bridgmanite from the third-order EOS fit is further discussed in supporting information S1.

3.2. Aggregate Elastic Properties of MgSiO₃ Bridgmanite

At each experimental pressure point, the adiabatic bulk (K_S) and shear moduli (G) have been calculated from the c_{ij} values in the Reuss and Voigt bounds (supporting information S1) and are reported in Table 1. The elastic moduli were then fitted with a third-order finite strain EOS (Stixrude & Lithgow-Bertelloni, 2005) to obtain K_{S0} , G_0 , K'_{S0} , and G'_0 (Table 2). While the third-order fits of the Voigt bulk and shear moduli, as well as the Reuss bulk modulus, have only small residuals relative to experimental data points (i.e., typically less than 0.5 GPa), there is a change in the slope of the Reuss bound of the shear modulus (G_R) at $\rho \sim 4.54$ g cc⁻¹ (i.e., 35 GPa). This is apparent from the systematic deviations in the fitting residual at both low and high densities (i.e., pressures) (Figure S2a, inset). This subtle change in the slope of the Reuss shear modulus occurs in the pressure interval where the shear wave anisotropy of MgSiO₃ bridgmanite shows a minimum, as already pointed out by Karki et al. (1997), and G_V and G_R tend to converge. At densities higher than 4.54 g cc⁻¹, the two bounds start to diverge again (Figure S2c) as the shear wave anisotropy of bridgmanite increases. One possible explanation for this behavior is that it results from a change in the response of octahedral tilting and polyhedral distortion of the bridgmanite structure with pressure, i.e., under an

isotropic stress environment (Reuss bound), for which corroborating evidence can be found in the evolution of lattice strain components for MgSiO₃ bridgmanite. Lattice strain components for the orthorhombic perovskite-type structure of bridgmanite can be simply calculated from unit cell parameters and describe the extent of lattice distortion with respect to a cubic perovskite structure, as described in previous studies (Boffa Ballaran et al., 2012; Carpenter, 2007; Carpenter et al., 2001). Of the three strain components, the tetragonal strain (e_{tx}), which is sensitive to both the degree of octahedral tilting and A site distortion, has also been shown to change in slope at ~ 35 GPa (Boffa Ballaran et al., 2012) as shown in Figure S3. We argue that the change in slope of G_R may, therefore, be detected from the change in the distortion mechanism of the perovskite structure with pressure relative to an undeformed cubic perovskite. It should be noted that this behavior of G_R results from a combination of pressure dependencies of the individual c_{ij} s, through the matrix inversion needed to obtain the compliances (s_{ij}) to calculate the Reuss bound, and does not mean that these dependencies are not well described by a third-order finite strain equation.

To better describe the change in slope of G_R , we fitted a fourth-order EOS to our shear moduli. To do so, we fixed the value of K_{S0} , K'_{S0} , as well as K''_{S0} (value implied by a third-order truncation of K , see supporting information S1) which can be determined independently from K - V data, and refined only the shear modulus G_0 and its derivatives G'_0 and G''_0 . A similar situation, where a higher truncation order for G is required with respect to K , was observed before in MgO (Zha et al., 2000). Alternatively, it is possible to fit two separate third-order EOS below 30 GPa and above 50 GPa to the same shear moduli dataset (Figure S2b), assuming two distinct shear mechanisms, as justified by the change in the slope of e_{tx} with pressure (Figure S3). The two fitting strategies are indistinguishable within uncertainty (Figure S2b). Fitting parameters of third- and fourth-order EOS are reported in Table 2.

3.3. Absolute Pressure Determination

One of the advantages of conducting elasticity and density measurements simultaneously on the same sample is that pressure can be determined without using any secondary pressure scale (e.g., ruby or Sm:YAG). The absolute pressure (P_{abs}) can be determined by integration of the isothermal bulk modulus in the Reuss bound and the volume over a certain volume range:

$$P_{abs} = \int_V^{V_0} \frac{K_{TR}(V)}{V} dV = 3K_{TR0}f(1+2f)^{\frac{5}{2}} \left[1 + \frac{3}{2}(K'_{TR0} - 4)f \right] \quad (3)$$

where K_{TR} is the Reuss isothermal bulk modulus, K_{TR0} is its value at ambient conditions and K'_{TR0} its pressure derivative. Using the relations $K_{SR} = K_{TR}(1 + \alpha\gamma T)$ and $\alpha = \gamma C_V / K_{TR} V$, we converted our experimentally determined K_{SR} into K_{TR} and calculated K_{TR0} and K'_{TR0} by fitting a third-order Birch-Munraghan EOS to our K_T - V data. Thermoelastic parameters used for the conversion of K_{SR} to K_{TR} at high pressure are reported in Table S2. The absolute pressure was then determined using experimentally measured volumes, and our $K_{TR0} = 254.5(4)$ GPa and $K'_{TR0} = 3.73(2)$. The deviation of P_{abs} from the ruby pressure scale is virtually zero at pressures below 40 GPa and increases to 1–5 GPa at the highest pressure achieved (Figure S4) depending on the employed pressure calibration for the ruby fluorescence (Dewaele et al., 2004; Jacobsen et al., 2008; Mao et al., 1986). The best agreement is found with the pressure scale determination of Jacobsen et al., (2008). For comparison, we also fitted a third-order Birch-Munraghan EOS to the experimental bridgmanite unit cell volumes using pressures determined from the ruby pressure scale of Jacobsen et al. (2008), and the EOSFit software (Angel et al., 2014; Gonzalez-Platas et al., 2016). The obtained fitting parameters of $K_{T0} = 255(10)$ GPa and $K'_{T0} = 3.8(2)$ are in good agreement with the values determined in the K_T - V fit reported above. Pressures calculated with our P - V EOS are in broad agreement, within uncertainty, with those calculated from single-crystal synchrotron X-ray diffraction measurements by Boffa Ballaran et al. (2012), powder diffraction measurements in the LVP by Katsura et al. (2009) and the recent computational study of Zhang et al. (2013) (Figure S5). On the other hand, powder X-ray diffraction data by Fiquet et al. (1998) and Tange et al. (2012) tend to overestimate pressures by more than 2 GPa already at 50 GPa. Tange et al. (2012) pointed out that the wide range of reported MgSiO₃ bridgmanite EOS parameters results from the use of different pressure scales and experimental techniques. Their MgSiO₃ bridgmanite EOS employed a primary MgO pressure scale calibrated with data sets where absolute pressure measurements were made (Tange, Nishi-

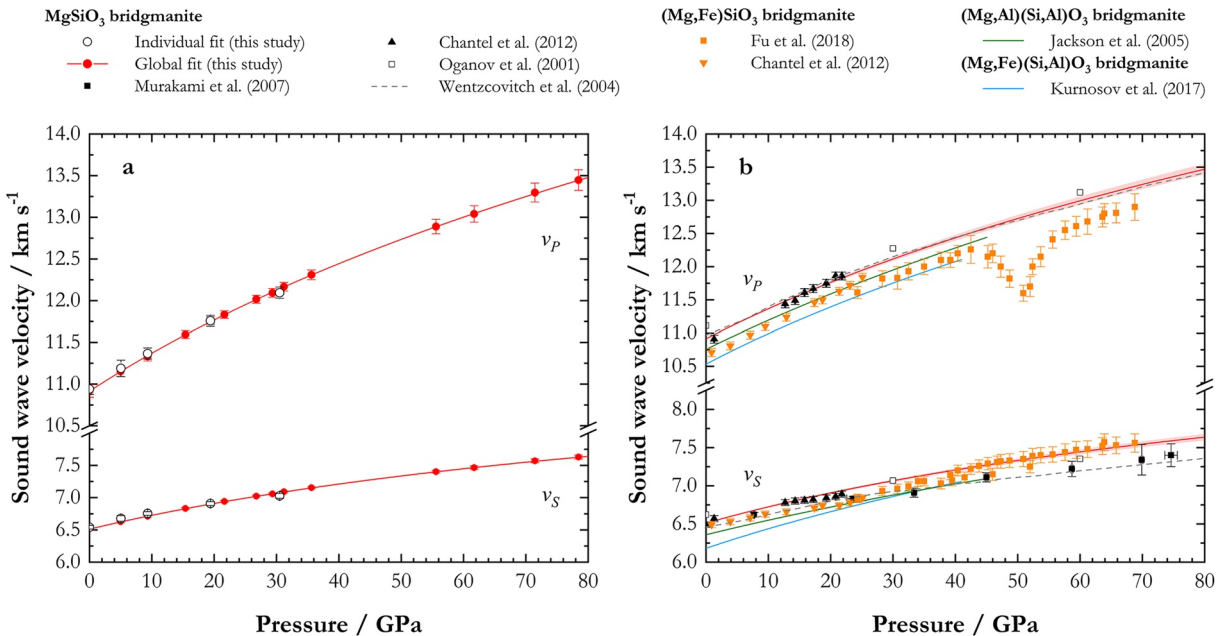


Figure 3. (a) Aggregate sound wave velocities of MgSiO₃ bridgmanite calculated from our single-crystal elasticity data, showing excellent agreement between individual fits (empty circles) and the global fit (red line and symbols). The error bars are calculated by propagating the experimental errors on density and elastic moduli. (b) Selected sound wave velocities of bridgmanite as a function of pressure from previous experimental and computational studies compared to the global fit. The shaded area indicates the propagated error on the fitting parameters and density. Murakami et al. (2007): Brillouin scattering on polycrystalline MgSiO₃ in DAC; Chantel et al. (2012): ultrasonic interferometry on MgSiO₃ and Mg_{0.95}Fe_{0.05}SiO₃ in LVP; Oganov et al. (2001): ab initio molecular dynamics on MgSiO₃; Wentzcovitch et al. (2004): first principle quasi-harmonic calculations on MgSiO₃; Fu et al. (2018): Brillouin scattering (v_s) and ISLS (v_p) on polycrystalline Mg_{0.96}Fe_{0.05}Si_{0.99}O₃ in DAC; Jackson et al. (2005): Brillouin scattering on polycrystalline Mg_{0.95}Al_{0.10}Si_{0.95}O₃ in DAC; Kurnosov et al. (2017): Brillouin scattering on single crystal Mg_{0.9}Fe_{0.1}Al_{0.1}Si_{0.9}O₃ in DAC.

hara, & Tsuchiya, 2009). However, the accuracy of such EOS measurements is reduced by both the error on the primary pressure scale and those on the volume measurements of the pressure marker. Our P_{abs} , on the other hand, is a primary pressure scale and has been derived from volume and elasticity measurements on single-crystals in a quasi-hydrostatic environment, which reduces the sources of systematic errors.

4. Discussion

Aggregate velocities of MgSiO₃ bridgmanite are computed from the Voigt–Reuss–Hill (VRH) average of the bulk and shear moduli (Hill, 1963) and show excellent agreement between individual fits and the global fit procedure (Figure 3a). A comparison of the global fit with previous experimental and computational elasticity studies is shown in Figure 3b. Ultrasonic interferometry data collected by Chantel et al. (2012) in a LVP are in good agreement with this study at pressures up to the top of the lower mantle, although the values of K_{S0} and K'_0 , 247(4) GPa and 4.5(2) respectively, would lead to an overestimation of v_p at deeper lower mantle conditions. Shear wave velocity data reported by Murakami et al. (2007) plot below the values determined in this study throughout the whole pressure range investigated. To make a fairer comparison, the v_s data of Murakami et al. (2007) were refitted using a consistent third-order truncation of the shear modulus EOS, as proposed by Chantel et al. (2016), rather than that derived from the fourth-order EOS of Davies and Dziewonski (1975), where Murakami et al. (2007) simply assumed that $K''_{S0} = 0$ and $G''_0 = 0$. Our fit gives $G_0 = 172.1(13)$ GPa and $G'_0 = 1.70(3)$, instead of $G_0 = 172.9(15)$ GPa and $G'_0 = 1.56(4)$, only partially lifting the difference in pressure derivatives between Murakami et al. (2007) and this study. The lower G'_0 compared to our measurements [$G'_{OV} = 1.86(1)$, $G'_{OR} = 1.81(3)$] may be due to the fact that Murakami et al. (2007) used a polycrystalline sample which may be subject to the development of preferred orientation during compression. It is important to note that Murakami et al. (2007) synthesized their polycrystalline bridgmanite sample in situ by laser heating a MgSiO₃ gel. In these experiments, it is difficult to control the crystal size of the synthesized products, which rarely exceeds a hundred nanometers. Such small crystallite

sizes can potentially trigger nonnegligible scattering from grain boundaries, causing sound velocity softening even at high pressure (Marquardt et al., 2011). This effect was reported to be particularly pronounced on the shear modulus of the polycrystalline aggregate, which, in the case of MgO, can be reduced by 1%–2% even when the crystal size is 500 nm (Marquardt et al., 2011). A grain size of 100 nm, for example, could therefore potentially explain the 3%–4% difference in shear wave velocities observed between our data set and that of Murakami et al. (2007).

Longitudinal wave velocities obtained in the computational studies of Oganov et al. (2001) and Wentzcovitch et al. (2004) are in reasonable agreement with our data at deep mantle conditions, as well as the shear wave velocities reported by Oganov et al. (2001). On the other hand, shear wave velocities reported by Wentzcovitch et al. (2004) are smaller by more than 3% at deep lower mantle pressure and close to the experimental results of Murakami et al. (2007). Based on their velocity data and previous static compression experiments Murakami et al. (2007, 2012) argued that a perovskite-rich (at least 93 volume %) lower mantle is required to match 1D seismic velocity models. Our elasticity data, instead, suggest that the shear modulus of bridgmanite is 3% stiffer than the values reported by Murakami et al. (2007) at mid lower mantle pressures. Therefore, the addition of softer materials (i.e., ferropericlase) is required to explain the slower v_S of the lower mantle assemblage, pointing toward a bulk composition that is more compatible with that of the upper mantle.

4.1. Effect of Chemistry on the Elasticity of Bridgmanite

The effect of Fe and Al on the compressional and shear wave velocities of bridgmanite has been investigated in several previous studies by means of Brillouin scattering, ISLS and ultrasonic interferometry (Chantel et al., 2012; Fu et al., 2018, 2019; Jackson et al., 2005; Kurnosov et al., 2017). A comparison between velocity data for MgSiO₃ bridgmanite from this study with selected previous studies, summarized in Table S1, is shown in Figure 3b. Chantel et al. (2012) reported that the incorporation of Fe in bridgmanite decreases its sound velocities relative to MgSiO₃. Despite showing much larger K'_0 (4.7) and lower G'_0 (1.56) than values reported here, sound velocities measured by Chantel et al. (2012) plot subparallel to the MgSiO₃ bridgmanite samples measured in this study. Recently, Fu et al. (2018) used Brillouin scattering and ISLS to further investigate the sound velocity of Mg_{0.96}Fe_{0.04}Si_{0.99}O₃ bridgmanite in DAC up to 70 GPa. The v_P of Fe-bearing bridgmanite is subparallel to the MgSiO₃ endmember presented in this study, except between 40 and 60 GPa, where a spin crossover of Fe³⁺ in the B site of bridgmanite is proposed to take place causing a drop in v_P . Note that at the onset of the spin crossover, the slope of the v_S increases and becomes slightly larger than that of MgSiO₃. Jackson et al. (2005) studied the effect of the AlAlO₃ component on the aggregate acoustic velocities of bridgmanite using Brillouin scattering in a DAC. Incorporation of 0.05 Al atoms in both A and B sites of the bridgmanite structure seems to decrease both v_P and v_S (Jackson et al., 2005), but does not appear to affect their pressure dependence compared to the MgSiO₃ endmember reported in this study. On the other hand, the incorporation of the FeAlO₃ component decreases acoustic velocities at ambient conditions and causes an increase in their pressure derivatives (Kurnosov et al., 2017). In particular, the slope of the shear wave velocity for 10 mol% FeAlO₃ bridgmanite is considerably higher than that measured for MgSiO₃ (Kurnosov et al., 2017). The decrease of both v_P and v_S in Fe-bearing Al-free bridgmanite at ambient conditions can be mainly attributed to the increase in density due to incorporation of Fe in the structure (Fu et al., 2018). On the other hand, Al incorporation in the B-site of bridgmanite increases the volume of the octahedral site causing an increase in its compressibility, which results in a lower bulk elastic moduli for Fe, Al-bearing bridgmanite (Kurnosov et al., 2017).

4.2. Elastic Anisotropy

The elastic properties of MgSiO₃ bridgmanite determined in this study at ambient conditions are in overall good agreement with previously reported values by Sinogeikin et al. (2004) in terms of both elastic anisotropy (Figure S6) and average properties (Table S1). The stiffest elastic component of MgSiO₃ bridgmanite at all pressures investigated in this study is the c_{22} , while the c_{11} and c_{33} show a crossover at ~15 GPa (Figure S1) with c_{33} becoming stiffer than c_{11} . The off-diagonal components c_{13} and c_{23} have very similar slopes throughout the whole pressure range investigated in this study, while the c_{12} is much steeper (Figure S1). A similar behavior was observed for FeAlO₃-bearing bridgmanite by Kurnosov et al. (2017). Among the shear

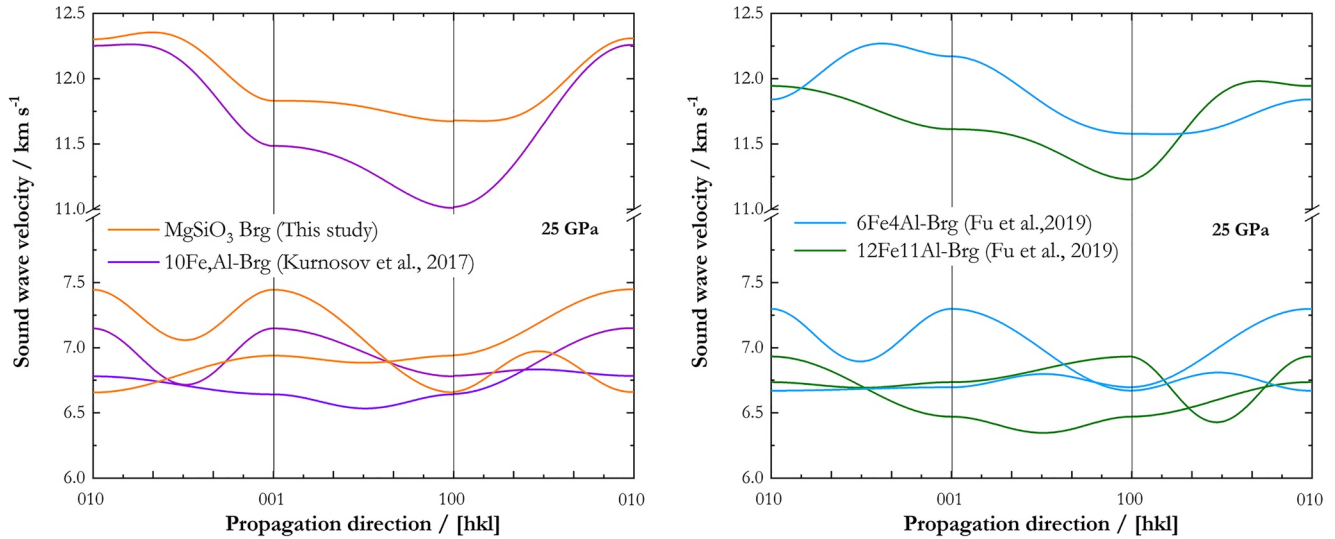


Figure 4. Dispersion curves of bridgmanite at 25 GPa. This study: MgSiO_3 (orange line) c_{ij} calculated from finite strain third-order EOS; Kurnosov et al. (2017): 10 mol% FeAlO_3 (purple line), c_{ij} calculated from finite strain third-order EOS; Fu et al. (2019): Fe_6Al_4 -Brg (cyan line) and $\text{Fe}_{12}\text{Al}_{11}$ -Brg (green line), c_{ij} at 25 GPa as reported in the mentioned paper.

components, the stiffest is the c_{44} , while the observed crossover in the c_{55} and c_{66} might be related to changes in the compression mechanism of individual Mg-O bonds with increasing pressure, affecting the shear mechanism of the A site of bridgmanite. While the c_{44} and c_{55} of FeAlO_3 -bearing bridgmanite measured by Kurnosov et al. (2017) are subparallel to MgSiO_3 bridgmanite, the slope of c_{66} is considerably higher. Once again, this is probably related to the higher degree of distortion of FeAlO_3 -bearing bridgmanite relative to the MgSiO_3 end member, which is described by the lattice strain term e_{ix} (Figure S3). Several first principle studies have also calculated the anisotropic elastic properties of MgSiO_3 bridgmanite at high pressure (Karki et al., 1997; Oganov et al., 2001; Wentzcovitch et al., 1998, 2004) and, in general, they show fairly good agreement with our results. While the diagonal components predicted by computational studies match well the values obtained in this study, the off-diagonal components tend to be more than 10% stiffer than our experimental values at mid-lower mantle pressures.

There are a number of inconsistencies that arise when the elastic stiffness components determined in this study and those determined by Kurnosov et al. (2017) are compared with values reported in the recent study of Fu et al. (2019) for bridgmanite solid solutions along the MgSiO_3 - FeAlO_3 join. The results of Fu et al. (2019) at 25 GPa indicate the relationship $c_{22} > c_{33} > c_{11}$ for a bridgmanite sample with composition $\text{Mg}_{0.89}\text{Fe}_{0.12}\text{Al}_{0.11}\text{Si}_{0.89}\text{O}_3$ ($\text{Fe}_{12}\text{Al}_{11}$), in agreement with this study and that of Kurnosov et al. (2017). However, they also report the relation $c_{33} > c_{22} > c_{11}$ for another bridgmanite sample with the composition $\text{Mg}_{0.96}\text{Fe}_{0.06}\text{Al}_{0.04}\text{Si}_{0.96}\text{O}_3$ (Fe_6Al_4). Based on their results, Fu et al. (2019) concluded that c_{22} increases while c_{11} and c_{33} decreases with increasing FeAlO_3 component. However, in determining these trends Fu et al. (2019) appear to have swapped the values of c_{22} and c_{33} calculated for the MgSiO_3 end member by Karki et al. (1997), who clearly report a c_{22} larger than c_{33} at all pressures. The trends as a function of FeAlO_3 component reported by Fu et al. (2019) appear therefore inconsistent when compared to experimental and theoretical studies reported in the literature (Karki et al., 1997; Kurnosov et al., 2017; Oganov et al., 2001; Wentzcovitch et al., 1998, 2004) (Figure S7). Moreover, the v_p anisotropy determined by Fu et al. (2019) for the Fe_6Al_4 and $\text{Fe}_{12}\text{Al}_{11}$ compositions at 25 GPa is quite different, even though the compositional change is relatively small (Figure 4). The v_p anisotropy determined by Kurnosov et al. (2017), on the other hand follows the same general trend as that of the MgSiO_3 end member measured in this study and deviates quite strongly from the results of Fu et al. (2019). At 35 GPa, the v_s anisotropy displayed by the Fe_6Al_4 and $\text{Fe}_{12}\text{Al}_{11}$ samples of Fu et al. (2019) becomes more similar (Figure S8), because of a major change in the anisotropy of the Fe_6Al_4 sample. This would imply a significant change in the compressibility mechanism for these samples over a pressure interval of only 10 GPa, which seems unlikely. Although the three studies employed Brillouin scattering to probe the v_s of the bridgmanite samples, the v_s anisotropy displayed by the

Fe6Al4 and Fe12Al11 samples of Fu et al. (2019) is not always in agreement with that of MgSiO₃ bridgmanite and FeAl-bearing bridgmanite samples measured in this study and by Kurnosov et al. (2017) respectively. For instance, at 25 GPa, the v_s of Fe12Al11 between [100] and [010] directions [i.e., (001) plane] looks similar to that of MgSiO₃ and Fe6Al4 between [010] and [001] [i.e., (100) plane], as shown in Figure 4, suggesting orientation problems. Note that the XRD, ISLS and Brillouin scattering measurements reported by Fu et al. (2019) were performed on three different setups and combined only afterward. On the other hand, XRD and Brillouin scattering measurements performed in this study and by Kurnosov et al. (2017) were performed on the same setup, without moving the sample. Further investigations on bridgmanite samples with intermediate compositions are therefore required to unequivocally solve this issue.

Using our high-pressure elastic stiffness components, the axial compressibility of MgSiO₃ bridgmanite can also be calculated for comparison purposes. The same relation between axial compressibilities $\beta_a > \beta_c > \beta_b$ (or axial moduli, $M_b > M_c > M_a$) can be observed in MgSiO₃ and FeAlO₃-bridgmanite through both elasticity and X-ray diffraction measurements independently (Boffa Ballaran et al., 2012; Kurnosov et al., 2017). We have used third-order linear EOS (Angel et al., 2014) to fit the unit cell parameters reported by Boffa Ballaran et al. (2012) for MgSiO₃ bridgmanite using the EosFit7-GUI software (Gonzalez-Platas et al., 2016). The axial moduli are calculated from the compliance components, s_{ij} , of MgSiO₃ bridgmanite obtained by inverting at each pressure the elastic stiffness tensor reported in this study. The axial moduli calculated in this way are in qualitative agreement with those calculated from the compression data reported in Boffa Ballaran et al. (2012), despite showing a less anisotropic behavior at high pressure and a smaller M_b (Figure S9). The axial moduli calculated from our elasticity measurements are also in fair agreement with computational studies (Oganov et al., 2001; Wentzcovitch et al., 1998, 2004) which reproduce well the axial compressibility of Boffa Ballaran et al. (2012) (Figure S9). Larger values of M_b observed at high pressure by Boffa Ballaran et al. (2012) may be explained by the larger calculated K'_{T0} relative to this study, which is most likely due to the different pressure scales employed.

5. A Mineral Physics Model for the Lower Mantle

Using previously published parameters for the thermal EOS of MgSiO₃ bridgmanite along with elasticity data for other components of the lower mantle, a mineral physical model can be constructed to predict seismic wave velocities for a given bulk mantle composition, which can then be compared with 1D seismic reference models (Dziewonski & Anderson, 1981; Kennett et al., 1995). Currently such a model can only be preliminary as the phase equilibria and EOS data required to model a complex mantle composition throughout the lower mantle are not available. Without more accurate knowledge, for example, of how the proportions and site occupancies of Fe³⁺ and Al in bridgmanite change with pressure, their inclusion in such a model introduces more uncertainty than they likely resolve. However, as uncertainties rise with the complexity of the model, a comparison with simpler chemical models allows factors to be identified that may be important in a suitably realistic model of the mantle.

Seismic wave velocities were computed as a function of depth for a primitive mantle composition (McDonough & Rudnick, 1998) consisting of bridgmanite, ferropericlase and Ca-perovskite in the CaO-MgO-SiO₂ (CMS) and CaO-FeO-MgO-SiO₂ (CFMS) systems. Mass fractions of Al₂O₃, Cr₂O₃, and TiO₂ were added to SiO₂. Calculations were performed using the formalism of Stixrude & Lithgow-Bertelloni (2011, 2005) to determine mineral compositions (in the CFMS system), seismic velocities and the adiabatic temperature profile, assuming a temperature of 1,960 K at 24 GPa (Katsura et al., 2010). In the light of new experimental results on the elastic properties of MgSiO₃ bridgmanite presented in this study, as well as of cubic Ca-perovskite (Gréaux et al., 2019), we decided to update the list of thermoelastic parameters presented in Stixrude & Lithgow-Bertelloni (2011). The complete list of employed parameters is reported in Table S2. For comparison, the aggregate velocities for the CMFS phase assemblage were also calculated using the original set of thermoelastic parameters reported in Stixrude & Lithgow-Bertelloni (2011). Our calculated v_s are approx. 0.8% (top lower mantle) to 1.7% (bottom lower mantle) faster than those calculated with the parameters of Stixrude & Lithgow-Bertelloni (2011), while v_p ranges from 0.4% faster (top lower mantle) to 1.0% slower (bottom lower mantle).

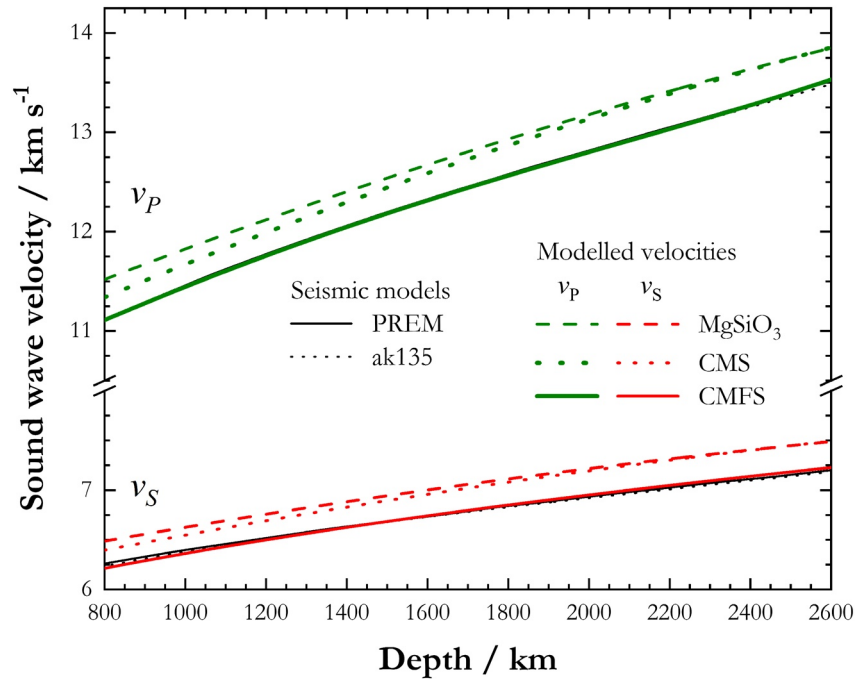


Figure 5. P- and S-wave velocities of MgSiO₃ bridgmanite (dashed colored lines) and lower mantle assemblages determined for a primitive mantle composition (McDonough & Rudnick, 1998) in the CMS (dotted colored lines) and CFMS (solid colored line) systems calculated along an adiabat with a temperature of 1,960 K at 660 km (Katsura et al., 2010). The difference between Voigt and Reuss bound of lower mantle assemblages, indicated by the thickness of the line, is about 40–60 m/s for v_p and 20–40 m/s for v_s . 1D seismic models PREM (solid black lines) and ak135 (dotted black lines) are shown for comparison.

A mass balance was used to determine component fractions and in the CFMS system the proportions of Fe²⁺ and Mg end members were constrained using a thermodynamic description of the distribution coefficient, K_D , defined as:

$$K_D = \left(X_{FeSiO_3}^{Brq} / X_{MgSiO_3}^{Brq} \right) / \left(X_{FeO}^{Fp} / X_{MgO}^{Fp} \right) \quad (4)$$

where X is the mole fraction of either bridgmanite (*Brq*) or ferropericalse (*Fp*) components. To model the effect of Fe-Mg nonideality of mixing, we used the parameters given by Nakajima et al. (2012). However, we calculate the standard state Gibbs free energy change for the corresponding exchange equilibrium (Equation 4) self consistently using the model of Stixrude & Lithgow-Bertelloni (2005, 2011). The model results in values of K_D which are in excellent agreement with recent multianvil studies performed up to ~60 GPa (Arimoto et al., 2019; Tange, Takahashi, et al., 2009) and in good agreement with some studies performed in the diamond anvil cell up to ~100 GPa (e.g., Auzende et al., 2008; Sakai et al., 2009), even though the Fe-Mg partitioning model does not explicitly account for the effect of an electronic spin transition of Fe²⁺ in ferropericalse. Using appropriate mineral component averaging schemes (Cottaar et al., 2014) the aggregate wave velocities in the Voigt and Reuss bound, as well as in Voigt-Reuss-Hill average, were then calculated. We make no allowance for the effects of attenuation in the calculation, which may further lower the calculated velocities (Cottaar et al., 2014) and the effects of iron spin transitions on the elastic properties have not been explicitly considered.

In Figure 5 velocities calculated along a mantle adiabat for a primitive mantle composition (McDonough & Rudnick, 1998) are compared in different systems with 1D seismic models (Dziewonski & Anderson, 1981; Kennett et al., 1995). Velocities for single-phase MgSiO₃ bridgmanite and the CMS model are faster than the seismic models; moreover, the CMS velocities also have distinctly steeper slopes, particularly for v_p (Figure 5). This arises from the slightly higher K'_0 of MgO (Kono et al., 2010) compared to bridgmanite. When Fe²⁺ is included in the CMFS model, however, there is reasonable agreement between the calculated

v_s and the seismic models throughout the entire lower mantle, with residuals never exceeding 0.6%. Even more striking agreement exists for v_p , which perfectly overlaps with PREM along the entire modeled depth interval within the Voigt and Reuss bounds. The improved agreement in the slope of v_p compared with the CMS model arises mainly because the Fe^{2+} -Mg K_D decreases with pressure, in line with experimental observations (Nakajima et al., 2012). As the proportion of the FeO endmember of ferropericlasite increases, both v_p and v_s decrease. Despite the excellent match between the slope of v_p for the CMFS phase assemblage and that of seismic models, it should be noted that the v_s slope is not in perfect agreement. This difference cannot be attributed to temperature, as it would similarly displace both v_p and v_s . This likely arises because the model does not include potential effects of Al or the spin crossover transition of Fe^{2+} in ferropericlasite, which would need to be considered in any meaningful comparison. As far as the spin crossover of Fe^{2+} in ferropericlasite is concerned (Kantor et al., 2006; Lin et al., 2005; Marquardt et al., 2018; Valencia-Cardona et al., 2017, and references therein), its effect on the elastic properties has not been considered at high pressure and temperature, but the CMFS model should at least capture any resulting effects on the Fe-Mg K_D because the available experimental data at pressure above the spin crossover transition are relatively well reproduced by our model. The incorporation of Al in bridgmanite is known to also raise the bridgmanite $\text{Fe}^{3+}/\Sigma\text{Fe}$ ratio to levels of ~ 0.5 (Frost et al., 2004), at least at conditions of the top of the lower mantle, due to the favorable substitution of an FeAlO_3 component. Fe^{3+} is likely produced in the lower mantle through charge disproportionation of Fe^{2+} that also leads to precipitation of Fe-rich alloy. As Al is added to bridgmanite half of the Fe^{2+} , therefore, becomes Fe^{3+} . The effect of adding an FeAlO_3 component to bridgmanite is twofold; on the one hand the incorporation of an FeAlO_3 component will lower the bulk and shear modulus of bridgmanite (Fu et al., 2019; Kurnosov et al., 2017) to some extent, while on the other hand the replacement of Fe^{2+} for Fe^{3+} will reduce the amount of Fe^{2+} that partitions into ferropericlasite, which will tend to raise the bulk and shear modulus. These combined effects may, therefore, tend to cancel out to some extent. However, quantifying this effect by incorporating it into a model for the entire bridgmanite stability field is not currently possible, because the definitive experiments to determine how the proportion of the bridgmanite FeAlO_3 component is likely to vary with depth in a primitive mantle composition have not yet been performed. It is quite possible, for example, that at higher pressures the proportion of the FeAlO_3 component decreases either due to changes in the Fe^{2+} disproportionation reaction, as proposed recently for silica saturated assemblages (Shim et al., 2017) or due to a raised preference for the AlAlO_3 and FeFeO_3 bridgmanite components. In addition to these problems, however, there is also a lack of high-pressure elasticity data on the effects of all bridgmanite components other than MgSiO_3 , as elasticity measurements performed so far on FeSiO_3 - and AlAlO_3 -bearing bridgmanite, for example, were conducted only on polycrystalline samples (Chantel et al., 2012; Fu et al., 2018; Jackson et al., 2005; Murakami et al., 2012).

In this study, we have shown that self-consistent measurements of X-ray diffraction and Brillouin scattering of single crystals can provide accurate and precise elastic parameters of bridgmanite up to pressures of the mid lower mantle. To improve the resolution of mineral physics models, more self-consistent single-crystal elasticity measurements at high-pressure and high-temperature are required to better constrain the effects of these bridgmanite components. Assumed thermal parameters and the effects of attenuation also need to be addressed. Reducing the chemical and thermal uncertainties should eventually allow more reliable complex mineral physics models to be developed through which the average bulk composition of the lower mantle, in addition to the nature of large-scale apparent heterogeneities, can ultimately be constrained.

Acknowledgments

The equipment for this research was supported through the ERC advanced grant number 227893 “DEEP” funded through the EU seventh Framework Program and by grant INST 91/315-1 FUGG and FR1555/11 from the DFG. The authors thank R. Njul for sample polishing and N. Miyajima and D. Wiesner for their assistance with the FIB device. Open access funding enabled and organized by Projekt DEAL.

Data Availability Statement

Sound velocity data used for c_{ij} calculation are available at: https://figshare.com/articles/dataset/sound_velocity_data_xlsx/14265176.

References

- Angel, R. J., & Finger, L. W. (2011). SINGLE: A program to control single-crystal diffractometers. *Journal of Applied Crystallography*, 44(1), 247–251. <https://doi.org/10.1107/S0021889810042305>
- Angel, R. J., Gonzalez-Platas, J., & Alvaro, M. (2014). EosFit7c and a Fortran module (library) for equation of state calculations. *Zeitschrift Fur Kristallographie*, 229(5), 405–419. <https://doi.org/10.1515/zkri-2013-1711>

- Arimoto, T., Irifune, T., Nishi, M., Tange, Y., Kunimoto, T., & Liu, Z. (2019). Phase relations of MgSiO₃-FeSiO₃ system up to 64 GPa and 2300 K using multianvil apparatus with sintered diamond anvils. *Physics of the Earth and Planetary Interiors*, 295, 106297. <https://doi.org/10.1016/j.pepi.2019.106297>
- Auzende, A.-L., Badro, J., Ryerson, F. J., Weber, P. K., Fallon, S. J., Addad, A., et al. (2008). Element partitioning between magnesium silicate perovskite and ferroperricline: New insights into bulk lower-mantle geochemistry. *Earth and Planetary Science Letters*, 269(1–2), 164–174. <https://doi.org/10.1016/j.epsl.2008.02.001>
- Ballaran, T. B., Kurnosov, A., Glazyrin, K., Frost, D. J., Merlini, M., Hanfland, M., & Caracas, R. (2012). Effect of chemistry on the compressibility of silicate perovskite in the lower mantle. *Earth and Planetary Science Letters*, 333–334(334), 181–190. <https://doi.org/10.1016/j.epsl.2012.03.029>
- Ballmer, M. D., Houser, C., Hermlund, J. W., Wentzcovitch, R. M., & Hirose, K. (2017). Persistence of strong silica-enriched domains in the Earth's lower mantle. *Nature Geoscience*, 10(3), 236–240. <https://doi.org/10.1038/ngeo2898>
- Boehler, R., & De Hantsetters, K. (2004). New anvil designs in diamond-cells. *High Pressure Research*, 24(3), 391–396. <https://doi.org/10.1080/08957950412331323924>
- Buchen, J. (2018). *The elastic properties of wadsleyite and stishovite at high pressures*. Ph.D. Thesis. Retrieved from <https://epub.uni-bayreuth.de/4410/>
- Carpenter, M. A. (2007). Elastic anomalies accompanying phase transitions in (Ca,Sr)TiO₃ perovskites: Part I. Landau theory and a calibration for SrTiO₃. *American Mineralogist*, 92(2–3), 309–327. <https://doi.org/10.2138/am.2007.2295>
- Carpenter, M. A., Becerro, A. I., & Seifert, F. (2001). Strain analysis of phase transitions in (Ca,Sr)TiO₃ perovskites. *American Mineralogist*, 86(3), 348–363. <https://doi.org/10.2138/am-2001-2-319>
- Chantel, J., Frost, D. J., McCammon, C. A., Jing, Z., & Wang, Y. (2012). Acoustic velocities of pure and iron-bearing magnesium silicate perovskite measured to 25 GPa and 1200 K. *Geophysical Research Letters*, 39, L19307. <https://doi.org/10.1029/2012GL053075>
- Chantel, J., Manthilake, G. M., Frost, D. J., Beyer, C., Ballaran, T. B., Jing, Z., & Wang, Y. (2016). Elastic wave velocities in polycrystalline Mg₃Al₂Si₃O₁₂-pyrope garnet to 24 GPa and 1300 K. *American Mineralogist*, 101(4), 991–997. <https://doi.org/10.2138/am-2016-5335>
- Cottaar, S., Heister, T., Rose, L., & Unterborn, C. (2014). BurnMan: A lower mantle mineral physics toolkit. *Geochemistry, Geophysics, Geosystems*, 15, 1164–1179. <https://doi.org/10.1002/2013GC005122>
- Davies, G. F., & Dziewonski, A. M. (1975). Homogeneity and constitution of the earth's lower mantle and outer core. *Physics of the Earth and Planetary Interiors*, 10(4), 336–343. [https://doi.org/10.1016/0031-9201\(75\)90060-6](https://doi.org/10.1016/0031-9201(75)90060-6)
- Dewaele, A., Loubeyre, P., & Mezouar, M. (2004). Equations of state of six metals above 94 GPa. *Physical Review B: Condensed Matter and Materials Physics*, 70(9), 094112. <https://doi.org/10.1103/PhysRevB.70.094112>
- Dziewonski, A. M., & Anderson, D. L. (1981). Preliminary reference Earth model. *Physics of the Earth and Planetary Interiors*, 25(4), 297–356. [https://doi.org/10.1016/0031-9201\(81\)90046-7](https://doi.org/10.1016/0031-9201(81)90046-7)
- Elkins-Tanton, L. T. (2012). Magma oceans in the inner solar system. *Annual Review of Earth and Planetary Sciences*, 40, 113–139. <https://doi.org/10.1146/annurev-earth-042711-105503>
- Every, A. G. (1980). General closed-form expressions for acoustic waves in elastically anisotropic solids. *Physical Review B: Condensed Matter*, 22(4), 1746–1760. <https://doi.org/10.1103/PhysRevB.22.1746>
- Fiquet, G., Andraut, D., Dewaele, A., Charpin, T., Kunz, M., & Häusermann, D. (1998). P-V-T equation of state of MgSiO₃ perovskite. *Physics of the Earth and Planetary Interiors*, 105(1–2), 21–31. [https://doi.org/10.1016/S0031-9201\(97\)00077-0](https://doi.org/10.1016/S0031-9201(97)00077-0)
- Fiquet, G., Dewaele, A., Andraut, D., Kunz, M., & Le Bihan, T. (2000). Thermoelastic properties and crystal structure of MgSiO₃ perovskite at lower mantle pressure and temperature conditions. *Geophysical Research Letters*, 27(1), 21–24. <https://doi.org/10.1029/1999GL008397>
- Frost, D. J., Liebske, C., Langenhorst, F., McCammon, C. A., Trønnes, R. G., & Rubie, D. C. (2004). Experimental evidence for the existence of iron-rich metal in the Earth's lower mantle. *Nature*, 428, 409–412. <https://doi.org/10.1029/2003JC000964>
- Fu, S., Yang, J., Tsujino, N., Okuchi, T., Purevjav, N., & Lin, J.-F. (2019). Single-crystal elasticity of (Al, Fe)-bearing bridgmanite and seismic shear wave radial anisotropy at the topmost lower mantle. *Earth and Planetary Science Letters*, 518, 116–126. Retrieved from <https://www.sciencedirect.com/science/article/pii/S0012821X19302274>
- Fu, S., Yang, J., Zhang, Y., Okuchi, T., McCammon, C., Kim, H.-I., et al. (2018). Abnormal Elasticity of Fe-Bearing Bridgmanite in the Earth's Lower Mantle. *Geophysical Research Letters*, 45, 4725–4732. <https://doi.org/10.1029/2018GL077764>
- Gonzalez-Platas, J., Alvaro, M., Nestola, F., & Angel, R. (2016). EosFit7-GUI: A new graphical user interface for equation of state calculations, analyses and teaching. *Journal of Applied Crystallography*, 49(4), 1377–1382. <https://doi.org/10.1107/s1600576716008050>
- Gréaux, S., Irifune, T., Higo, Y., Tange, Y., Arimoto, T., Liu, Z., & Yamada, A. (2019). Sound velocity of CaSiO₃ perovskite suggests the presence of basaltic crust in the Earth's lower mantle. *Nature*. <https://doi.org/10.1038/s41586-018-0816-5>
- Hill, R. (1963). Elastic properties of reinforced solids: Some theoretical principles. *Journal of the Mechanics and Physics of Solids*, 11(5), 357–372. [https://doi.org/10.1016/0022-5096\(63\)90036-X](https://doi.org/10.1016/0022-5096(63)90036-X)
- Irifune, T. (1994). Absence of an aluminous phase in the upper part of the Earth's lower mantle. *Nature*, 370(6485), 131–133. <https://doi.org/10.1038/370131a0>
- Irifune, T., Shinmei, T., McCammon, C. A., Miyajima, N., Rubie, D. C., & Frost, D. J. (2010). Iron Partitioning and Density Changes of Pyrolite in Earth's Lower Mantle. *Science*, 327(5962), 193–195. <https://doi.org/10.1126/science.1181443>
- Ishii, T., Kojitani, H., & Akaogi, M. (2011). Post-spinel transitions in pyrolite and Mg₂SiO₄ and akimotoite-perovskite transition in MgSiO₃: Precise comparison by high-pressure high-temperature experiments with multi-sample cell technique. *Earth and Planetary Science Letters*, 309(3–4), 185–197. <https://doi.org/10.1016/j.epsl.2011.06.023>
- Jackson, J. M., Zhang, J., Shu, J., Sinogeikin, S. V., & Bass, J. D. (2005). High-pressure sound velocities and elasticity of aluminous Mg-SiO₃ perovskite to 45 GPa: Implications for lateral heterogeneity in Earth's lower mantle. *Geophysical Research Letters*, 32(21), L21305. <https://doi.org/10.1029/2005GL023522>
- Jacobsen, S. D., Holl, C. M., Adams, K. A., Fischer, R. A., Martin, E. S., Bina, C. R., et al. (2008). Compression of single-crystal magnesium oxide to 118 GPa and a ruby pressure gauge for helium pressure media. *American Mineralogist*, 93(11–12), 1823–1828. <https://doi.org/10.2138/am.2008.2988>
- Kantor, I., Prakapenka, V., Kantor, A., Dera, P., Kurnosov, A., Sinogeikin, S., et al. (2012). BX90: A new diamond anvil cell design for X-ray diffraction and optical measurements. *Review of Scientific Instruments*, 83(12), 125102. <https://doi.org/10.1063/1.4768541>
- Kantor, I. Y., Dubrovinsky, L. S., & McCammon, C. A. (2006). Spin crossover in (Mg,Fe)O: A Mössbauer effect study with an alternative interpretation of x-ray emission spectroscopy data. *Physical Review B*, 73(10), 100101. <https://doi.org/10.1103/PhysRevB.73.100101>
- Karki, B. B., Stixrude, L., Clark, S. J., Warren, M. C., Ackland, G. J., & Crain, J. (1997). Elastic properties of orthorhombic MgSiO₃ perovskite at lower mantle pressures. *American Mineralogist*, 82(5–6), 635–638. <https://doi.org/10.2138/am-1997-5-623>

- Katsura, T., Yokoshi, S., Kawabe, K., Shatskiy, A., Manthilake, M. A. G. M., Zhai, S., et al. (2009). P-V-T relations of MgSiO₃ perovskite determined by in situ X-ray diffraction using a large-volume high-pressure apparatus. *Geophysical Research Letters*, 36, L01305. <https://doi.org/10.1029/2008GL035658>
- Katsura, T., Yoneda, A., Yamazaki, D., Yoshino, T., Ito, E., Suetsugu, D., et al. (2010). Adiabatic temperature profile in the mantle. *Physics of the Earth and Planetary Interiors*, 183(1–2), 212–218. <https://doi.org/10.1016/j.pepi.2010.07.001>
- Kennett, B. L. N., Engdahl, E. R., & Buland, R. (1995). Constraints on seismic velocities in the Earth from traveltimes. *Geophysical Journal International*, 122(1), 108–124. <https://doi.org/10.1111/j.1365-246X.1995.tb03540.x>
- King, H. E., & Finger, L. W. (1979). Diffracted beam crystal centering and its application to high-pressure crystallography. *Journal of Applied Crystallography*, 12(4), 374–378. <https://doi.org/10.1107/S0021889879012723>
- Kono, Y., Irifune, T., Higo, Y., Inoue, T., Barnhoorn, A., Suetsugu, D., et al. (2010). P-V-T relation of MgO derived by simultaneous elastic wave velocity and in situ X-ray measurements: A new pressure scale for the mantle transition region. *Physics of the Earth and Planetary Interiors*, 183(1–2), 196–211. <https://doi.org/10.1016/j.pepi.2010.03.010>
- Kurnosov, A., Kantor, I., Boffa-Ballaran, T., Lindhardt, S., Dubrovinsky, L., Kuznetsov, A., & Zehnder, B. H. (2008). A novel gas-loading system for mechanically closing of various types of diamond anvil cells. *Review of Scientific Instruments*, 79(4), 045110. <https://doi.org/10.1063/1.2902506>
- Kurnosov, A., Marquardt, H., Frost, D. J., Ballaran, T. B., & Ziberna, L. (2017). Evidence for a Fe³⁺-rich pyrolytic lower mantle from (Al, Fe)-bearing bridgmanite elasticity data. *Nature*, 543(7646), 543–546. <https://doi.org/10.1038/nature21390>
- Lin, J.-F., Struzhkin, V. V., Jacobsen, S. D., Shen, G., Prakapenka, V. B., Mao, H.-K., & Hemley, R. J. (2005). X-ray emission spectroscopy with a laser-heated diamond anvil cell: A new experimental probe of the spin state of iron in the Earth's interior. *Journal of Synchrotron Radiation*, 12, 637–641. <https://doi.org/10.1107/S0909049505020741>
- Mao, H. K., Xu, J., & Bell, P. M. (1986). Calibration of the ruby pressure gauge to 800 kbar under quasi-hydrostatic conditions. *Journal of Geophysical Research*, 91(B5), 4673. <https://doi.org/10.1029/jb091ib05p04673>
- Marquardt, H., Buchen, J., Mendez, A. S. J., Kurnosov, A., Wendt, M., Rothkirch, A., et al. (2018). Elastic softening of (Mg 0.8 Fe 0.2)O Ferropericlase across the iron spin crossover measured at seismic frequencies. *Geophysical Research Letters*, 45, 6862–6868. <https://doi.org/10.1029/2018GL077982>
- Marquardt, H., Gleason, A., Marquardt, K., Speziale, S., Miyagi, L., Neusser, G., et al. (2011). Elastic properties of MgO nanocrystals and grain boundaries at high pressures by Brillouin scattering. *Physical Review B: Condensed Matter and Materials Physics*, 84(6), 1–9. <https://doi.org/10.1103/PhysRevB.84.064131>
- McDonough, W. F., & Rudnick, R. L. (1998). Chapter 4. Mineralogy and composition of the upper mantle. In R. Hemley, (Ed.), *Ultra-high-pressure mineralogy: Physics and chemistry of the Earth's deep interior*, *Reviews in Mineralogy* 37 (pp. 139–164). Mineralogical Society of America.
- Murakami, M., Ohishi, Y., Hirao, N., & Hirose, K. (2012). A perovskitic lower mantle inferred from high-pressure, high-temperature sound velocity data. *Nature*, 485(7396), 90–94. <https://doi.org/10.1038/nature11004>
- Murakami, M., Sinogeikin, S., Hellwig, H., Bass, J., & Li, J. (2007). Sound velocity of MgSiO₃ perovskite to Mbar pressure. *Earth and Planetary Science Letters*, 256(1–2), 47–54. <https://doi.org/10.1016/j.epsl.2007.01.011>
- Nakajima, Y., Frost, D. J., & Rubie, D. C. (2012). Ferrous iron partitioning between magnesium silicate perovskite and ferropericlase and the composition of perovskite in the Earth's lower mantle. *Journal of Geophysical Research*, 117(8), B08201. <https://doi.org/10.1029/2012jb009151>
- Oganov, A. R., Brodholt, J. P., & Price, G. D. (2001). Ab initio elasticity and thermal equation of state of MgSiO₃ perovskite. *Earth and Planetary Science Letters*, 184(3–4), 555–560. [https://doi.org/10.1016/S0012-821X\(00\)00363-0](https://doi.org/10.1016/S0012-821X(00)00363-0)
- Palme, H., & O'Neill, H. (2014). Cosmochemical Estimates of Mantle Composition In *Treatise on Geochemistry*. <https://doi.org/10.1016/B978-0-08-095975-7.00201-1>
- Poirier, J.-P. (1994). Light elements in the Earth's outer core: A critical review. *Physics of the Earth and Planetary Interiors*, 85(3–4), 319–337. [https://doi.org/10.1016/0031-9201\(94\)90120-1](https://doi.org/10.1016/0031-9201(94)90120-1)
- Ralph, R. L., & Finger, L. W. (1982). A computer-program for refinement of crystal orientation matrix and lattice-constants from diffractometer data with lattice symmetry constraints. *Journal of Applied Crystallography*, 15, 537–539. <https://doi.org/10.1107/S0021889882012539>
- Ringwood, A. E. (1962). A model for the upper mantle: 2. *Journal of Geophysical Research*, 67(11), 4473–4478. <https://doi.org/10.1029/jz067i011p04473>
- Sakai, T., Ohtani, E., Terasaki, H., Sawada, N., Kobayashi, Y., Miyahara, M., et al. (2009). Fe-Mg partitioning between perovskite and ferropericlase in the lower mantle. *American Mineralogist*, 94(7), 921–925. <https://doi.org/10.2138/am.2009.3123>
- Sandercock, J. R. (1982). *Trends in brillouin scattering: Studies of opaque materials, supported films, and central modes*. Springer. https://doi.org/10.1007/3540115137_6
- Schulze, K., Buchen, J., Marquardt, K., & Marquardt, H. (2017). Multi-sample loading technique for comparative physical property measurements in the diamond-anvil cell. *High Pressure Research*, 37(2), 159–169. <https://doi.org/10.1080/08957959.2017.1299719>
- Shim, S.-H., Grocholski, B., Ye, Y., Alp, E. E., Xu, S., Morgan, D., et al. (2017). Stability of ferrous-iron-rich bridgmanite under reducing midmantle conditions. *Proceedings of the National Academy of Sciences of the United States of America*, 114(25), 6468–6473. <https://doi.org/10.1073/pnas.1614036114>
- Sinogeikin, S. V., Zhang, J., & Bass, J. D. (2004). Elasticity of single crystal and polycrystalline MgSiO₃ perovskite by Brillouin spectroscopy. *Geophysical Research Letters*, 31, L06620. <https://doi.org/10.1029/2004gl019559>
- Speziale, S., Marquardt, H., & Duffy, T. S. (2014). Brillouin scattering and its application in geosciences. *Reviews in Mineralogy and Geochemistry*, 78(1), 543–603. <https://doi.org/10.2138/rmg.2014.78.14>
- Stixrude, L., & Lithgow-bertelloni, C. (2005). Thermodynamics of mantle minerals - I. Physical properties. *Physical Properties*, 162, 610–632. <https://doi.org/10.1111/j.1365-246X.2005.02642.x>
- Stixrude, L., & Lithgow-Bertelloni, C. (2011). Thermodynamics of mantle minerals - II. Phase equilibria. *Geophysical Journal International*, 184(3), 1180–1213. <https://doi.org/10.1111/j.1365-246X.2010.04890.x>
- Tange, Y., Kuwayama, Y., Irifune, T., Funakoshi, K. I., & Ohishi, Y. (2012). P-V-T equation of state of MgSiO₃ perovskite based on the MgO pressure scale: A comprehensive reference for mineralogy of the lower mantle. *Journal of Geophysical Research*, 117, B06201. <https://doi.org/10.1029/2011JB008988>
- Tange, Y., Nishihara, Y., & Tsuchiya, T. (2009). Unified analyses for P-V-T equation of state of MgO: A solution for pressure-scale problems in high P-T experiments. *Journal of Geophysical Research*, 114, B03208. <https://doi.org/10.1029/2008JB005813>

- Tange, Y., Takahashi, E., Nishihara, Y., Funakoshi, K. I., & Sata, N. (2009). Phase relations in the system MgO-FeO-SiO₂ to 50 GPa and 2000°C: An application of experimental techniques using multianvil apparatus with sintered diamond anvils. *Journal of Geophysical Research*, *114*(2), B02214. <https://doi.org/10.1029/2008JB005891>
- Tonks, W. B., & Melosh, H. J. (1993). Magma ocean formation due to giant impacts. *Journal of Geophysical Research*, *98*(E3), 5319–5333. <https://doi.org/10.1029/92JE02726>
- Trots, D. M., Kurnosov, A., Ballaran, T. B., Tkachev, S., Zhuravlev, K., Prakapenka, V., et al. (2013). The Sm: YAG primary fluorescence pressure scale. *Journal of Geophysical Research: Solid Earth*, *118*, 5805–5813. <https://doi.org/10.1002/2013JB010519>
- Trots, D. M., Kurnosov, A., Vasylechko, L., Berkowski, M., Boffa Ballaran, T., & Frost, D. J. (2011). Elasticity and equation of state of Li₂B₄O₇. *Physics and Chemistry of Minerals*, *38*(7), 561–567. <https://doi.org/10.1007/s00269-011-0428-1>
- Valencia-Cardona, J. J., Shukla, G., Wu, Z., Houser, C., Yuen, D. A., & Wentzcovitch, R. M. (2017). Influence of the iron spin crossover in ferropericlase on the lower mantle geotherm. *Geophysical Research Letters*, *44*, 4863–4871. <https://doi.org/10.1002/2017GL073294>
- Wänke, H. (1981). Constitution of terrestrial planets. *Philosophical Transactions of the Royal Society of London - Series A: Mathematical and Physical Sciences*, *303*, 287–302.
- Wentzcovitch, R. M., Karki, B. B., Cococcioni, M., & de Gironcoli, S. (2004). Thermoelastic Properties of MgSiO₃-Perovskite: Insights on the Nature of the Earth's Lower Mantle. *Physical Review Letters*, *92*(1), 4. <https://doi.org/10.1103/PhysRevLett.92.018501>
- Wentzcovitch, R. M., Karki, B. B., Karato, S., & Da Silva, C. R. S. (1998). High pressure elastic anisotropy of MgSiO₃ perovskite and geophysical implications. *Earth and Planetary Science Letters*, *164*(1–2), 371–378. [https://doi.org/10.1016/S0012-821X\(98\)00230-1](https://doi.org/10.1016/S0012-821X(98)00230-1)
- Whitfield, C. H., Brody, E. M., & Bassett, W. A. (1976). Elastic moduli of NaCl by Brillouin scattering at high pressure in a diamond anvil cell. *Review of Scientific Instruments*, *47*(8), 942–947. <https://doi.org/10.1063/1.1134778>
- Zha, C. S., Mao, H.-k., & Hemley, R. J. (2000). Elasticity of MgO and a primary pressure scale to 55 GPa. *Proceedings of the National Academy of Sciences*, *97*(25), 13494–13499. <https://doi.org/10.1073/pnas.240466697>
- Zhang, Z., Stixrude, L., & Brodholt, J. (2013). Elastic properties of MgSiO₃-perovskite under lower mantle conditions and the composition of the deep Earth. *Earth and Planetary Science Letters*, *379*, 1–12. <https://doi.org/10.1016/j.epsl.2013.07.034>

References From the Supporting Information

- Fischer, R. A., Campbell, A. J., Shofner, G. A., Lord, O. T., Dera, P., & Prakapenka, V. B. (2011). Equation of state and phase diagram of FeO. *Earth and Planetary Science Letters*, *304*(3–4), 496–502. <https://doi.org/10.1016/j.epsl.2011.02.025>
- Lin, J.-F., Mao, Z., Yang, J., & Fu, S. (2018). Elasticity of lower-mantle bridgmanite. *Nature*, *564*(7736), E18–E26. <https://doi.org/10.1038/s41586-018-0741-7>
- Melinger-Cohen, A., & Jeanloz, R. (2019). Finite strain analysis of shear and compressional wave velocities. *Journal of Geophysical Research: Solid Earth*, *124*, 11651–11677. <https://doi.org/10.1029/2019JB017868>
- Sinogeikin, S. V., & Bass, J. D. (2000). Single-crystal elasticity of pyrope and MgO to 20 GPa by Brillouin scattering in the diamond cell. *Physics of the Earth and Planetary Interiors*, *120*(1), 43–62. [https://doi.org/10.1016/S0031-9201\(00\)00143-6](https://doi.org/10.1016/S0031-9201(00)00143-6)
- Zha, C. S., Duffy, T. S., Downs, R. T., Mao, H. K., & Hemley, R. J. (1996). Sound velocity and elasticity of single-crystal forsterite to 16 GPa. *Journal of Geophysical Research*, *101*(8), 17535–17545. <https://doi.org/10.1029/96jb01266>